Regenerated cellulose/chitosan composite aerogel with highly efficient adsorption for anionic dyes

Shaochun He, Junting Li, Xundan Cao, Fei Xie, Hui Yang, Cheng Wang, Carla Bittencourt, Wenjiang Li

PII: S0141-8130(23)01961-X

DOI: https://doi.org/10.1016/j.ijbiomac.2023.125067

Reference: BIOMAC 125067

To appear in: *International Journal of Biological Macromolecules*

Received date: 11 March 2023

Revised date: 15 May 2023

Accepted date: 22 May 2023

Please cite this article as: S. He, J. Li, X. Cao, et al., Regenerated cellulose/chitosan composite aerogel with highly efficient adsorption for anionic dyes, *International Journal of Biological Macromolecules* (2023), https://doi.org/10.1016/j.ijbiomac.2023.125067

Regenerated cellulose/chitosan composite aerogel with highly efficient adsorption for anionic dyes

Shaochun He[a], Junting Li[a+], Xundan Cao[b], Fei Xie[a], Hui Yang[b], Cheng Wang[a], Carla Bittencourt[c], Wenjiang Li[a]*

[a]*School of Materials Science and Engineering, School of Chemistry and Chemical Engineering, Tianjin University of Technology, Tianjin 300384, China*

[b]*Zhejiang–California International Nanosystems Institute, Zhejiang University, Hangzhou 310012, People's Republic of China*

[c]*Chimie des Interactions Plasma-Surface, Université de Mons (UMONS), 20 Place du Parc, 7000 Mons, Belgium*

**To whom correspondence should be addressed. Tel: 0086-22-60214028; e-mail: liwj@tjut.edu.cn*

[+] *equal contribution to the first author*

Abstract: A novel reusable, high-compressible cotton regenerated cellulose/chitosan composite aerogel (RC/CSCA) was prepared using N-methylmorpholine-N-oxide (NMMO) as the green cellulose solvent, and glutaraldehyde (GA) as the crosslinking agent. The regenerated cellulose obtained from cotton pulp could chemically crosslink with chitosan and GA, to form a stable 3D porous structure. The GA played an essential role in preventing shrinkage and preserving the deformation recovery ability of RC/CSCA. Due to the ultralow density (13.92 mg/cm^3), thermal stability (above 300°C), and high porosity (97.36%), the positively charged RC/CSCA can be used as a novel biocomposite adsorbent for effective and selective removal of toxic anionic dyes from wastewater, showing an excellent adsorption capacity, environmental adaptability, and recyclability. The maximal adsorption capacity and removal efficiency of RC/CSCA for methyl orange (MO) was 742.68 mg/g and 95.83%.

Keywords: Regenerated cellulose; macroporous network; water purification; Selective adsorption; Reusability

1 Introduction

Environmental pollution has become a critical global concern of modern societies[1]. Mainly, wastewater contains a variety of carcinogenic and teratogenic pollutants, including some organic and inorganic harmful substances, partly not easily degradable in the environment, which would bring significant risks to water species and human beings[2]. Therefore, various methods, including adsorption technology, flocculation, photocatalysis, and bioremediation, have been developed for removing pollutants from wastewater[3-5]. Among them, the adsorption method is a promising strategy because of its low cost, high efficiency, and simple operation. Actually, various kinds of functional materials, such as carbon nanomaterials[6], zeolite[7], clay[8], and polystyrene[9], have been used as absorbents for water treatment. However, most adsorbents could not be widely used in practical applications due to low adsorption capacity, high cost, and non-biodegradable or non-recyclability. Therefore, it is still challenging to separate the diversified dyes that coexist in wastewater [10]. Therefore, developing novel adsorbents which can remove dyes effectively and selectively from wastewater but are also easily reusable, low-cost, and eco-friendly is still a great challenge.

As well known, besides the capillary effect, the surface functional groups and charge states of porous adsorbents play an essential role in the adsorption and separation of dyes from a solution[11]. For example, anionic dyes, mainly composed of azo and anthraquinone structures, are widely used colorants, which might be strongly absorbed by the porous adsorbents with positively charged[12-14].

In this context, abundant, renewable, degradable cellulose and chitosan have been widely used as aerogel adsorption materials to remove dyes from wastewater [10]. In particular, regenerated cellulose (RC) obtained via N-methylmorpholine-N-oxide (NMMO) physical dissolution has attracted much attention because its abundant hydroxyl groups are easily chemically modified [15, 16]. Moreover, NMMO, in which active N-O dipoles can break cellulose molecules' intrinsic hydrogen bond networks, may be recycled and reused as a "Green" solvent [17, 18]. However, the low adsorption capacity and poor recovery of pure cellulose aerogels limited its practical applications. Therefore, many strategies have been investigated to improve cellulose aerogel's adsorption property and recovery, such as surface chemistry modification, adding reinforcement materials, and loading organic or inorganic materials [19]. Recently, we reported on the synthesis of regenerated cellulose(RC) aerogel obtained from short cotton wool crosslinked with N, N'-methylenebisacrylamide (MBA), efficiently removing Congo red from water[20].On the other hand, due to abundant hydroxyl and amino groups on molecular chains as chelating agents or the positively charged groups, chitosan composites (CS) have been reported as absorbents to remove heavy metal ions and anionic dyes in wastewater[21-24]. However, chitosan is unstable and hydrolytic in an aqueous solution, preventing its practical applications as pure CS aerogel for water treatment [12].

Recently, many kinds of cellulose-chitosan composite aerogels have been reported, presenting enhanced mechanical properties, in which the swelling property of chitosan was also relieved in water.[23, 25-27]. For example: Do et al[28] reported

that TEMPO-oxidized pineapple leaf pulp-chitosan composite aerogel simultaneously adsorbed anionic and cationic dyes in water. However, as far as we know, less attention has been paid to developing a high-compressible and reusable cellulose/chitosan composite aerogel using the "Green" solvent of NMMO for effective and selectively removing anionic dyes from water.

Here, a novel reusable and high-compressible cotton regenerated cellulose/chitosan composite aerogel (RC/CSCA) were prepared via an environmentally friendly process, using NMMO as the green cellulose solvent, and glutaraldehyde (GA) as the crosslinking agent, in which RC obtained from cotton pulp could crosslink with chitosan via electrostatic and hydrogen bonding interactions between NH_3^+ and -OH groups, to form a stable 3D porous structure. The chemical crosslink of GA with RC and CS via amines or hydroxyl groups enhanced the structural stability of the 3D porous skeleton, refraining from shrinkage and retaining the deformation recovery ability of RC/CSCA. The chemical composition, structural, morphological, and mechanical stability of RC/CSCA were studied in detail. Owing to the ultralow density (13.92 mg/cm^3), thermal stability (above 300℃), and high porosity (97.36 %), the positively charged and highly compressible 3D porous RC/CSCA can be used as a novel biocomposite adsorbent for effective and selective removal of toxic anionic dyes from wastewater, showing an excellent adsorption capacity, environmental adaptability, and recyclability. The maximal adsorption capacity and removal efficiency of RC/CSCA for methyl orange (MO) was 742.68 mg/g and 95.83%. The low-cost, reusable, and compressible RC/CSCA as a novel

biobased-adsorbent presents a broad potential in dye wastewater treatment.

2 Experimental

2.1 Materials

Firstly, the cotton pulp (1.5 g) as the cellulose and ascorbic acid (0.03 g) as the antioxidant are successively added into 100 g of NMMO·H_2O solution in a double-layer glass reactor under vigorously stirring at 100℃ for 20 min under vacuum conditions. As a result, a uniform amber cellulose-NMMO mixture is obtained. Then, the dissolved cellulose solution is poured into the mold and solidified at room temperature. Finally, the cellulose hydrogel (RCH) is obtained after immersing the solid cellulose material in distilled water for 48 h and washing it several times to remove the NMMO solvent completely. A diagram of the preparation process of the regenerated cellulose hydrogel via NMMO solvent is shown in Fig.S1.

2.2 Regenerated cellulose hydrogel (RCH)

Firstly, the cotton pulp (1.5 g) as the cellulose and ascorbic acid (0.03 g) as the antioxidant were successively added into 100 g of NMMO·H_2O solution in a double-layer glass reactor under vigorously stirring at 100℃ for 20 min under vacuum conditions. The uniform amber cellulose-NMMO mixture was obtained. Then, the dissolved cellulose solution was poured into the mold and solidified at room temperature. Finally, the cellulose hydrogel (RCH) was obtained after immersing the solid cellulose material in distilled water for 48 h and washing it several times to remove the NMMO solvent completely. Diagram of the preparation process of

regenerated cellulose hydrogel via NMMO solvent is shown in Fig.S1.

2.3 Regenerated cellulose/chitosan composite aerogel (RC/CSCA)

The synthetic route of the RC/CSCA is shown in Schema 1. Firstly, 2 g of CS powder is dissolved in aqueous acetic acid (1 wt%) and stirred thoroughly at 25℃ for a CS transparent solution. Next, the above RCH is cut into small pieces and pulped with a high-speed mechanical shear at 15000r min^{-1} for 30 min to obtain a uniform RC suspension (15 mg mL^{-1}). And the RC suspension is mixed with different concentrations of chitosan solution and the glutaraldehyde (3 wt% of chitosan powder), continuously stirring in a water bath at 60℃ for 1 h to allow the constant interaction between the regenerated cellulose fibers, chitosan, and the glutaraldehyde molecules. Thus, the regenerated cellulose/chitosan composite (RC/CSC) is obtained. Finally, a pale-yellow soft mixture is obtained after degassing RC/CSC material in a vacuum oven for 20 min. After cooling to room temperature, the pale-yellow mixture is frozen in a refrigerator for 12h, followed by lyophilization at −55℃ for 48h in a vacuum (1 Pa). After washing with deionized water and ethanol to remove unreacted acetic acid and GA, the wetting aerogel is freeze-dried for subsequent analysis. The aerogels named RC/CSCA-1, RC/CSCA-2, RC/CSCA-3, and RC/CSCA-4 correspond to samples with RC:CS mass ratios of 3:1, 3:2, 1:1, and 3:4, respectively. For comparison, the pure RC aerogel (RCA), CS aerogel (CSA), and RC/CS composite aerogel without GA (RC/CSCA-0) were also prepared following the above method.

2.4 Characterization

The surface morphology and structure of prepared samples were observed using

a field emission scanning electron microscope (FE-SEM, FEI, USA). Fourier transform infrared spectra (FTIR, Perkin Elmer, USA) were recorded in the range of 4000-400 cm^{-1} to identify chemical functional groups. The crystallographic structure of the samples was studied by X-ray diffraction (XRD, D/Max2500pc, Rigaku) in the 2θ range of 5 to 60°. Thermogravimetric analysis (TG, 209F3A, NETZSCH) was used to assess the thermal stability of the samples and the proportion of volatile components. The tests were conducted in nitrogen at a heating rate of 10°C/min over a temperature range of 35-800°C. X-ray photoelectron spectroscopy (XPS; ESCALAB250Xi, THERMO SCIENTIFIC, UK) analyzed chemical bonding states and elemental composition. The compression unit Univert S2 (Cellscale, Canada) has a 200 kN load cell with a 2 mm/min compression speed. UV-Vis spectrophotometer (TU-1901, Beijing, China) for measuring the absorbance of dyes in aqueous solutions. The pH at the point of zero charges (PHPZC) is determined by the pH drift method [29]. While, the ethanol substitution method determined the average porosity of aerogels. Supplementary Information, Text S1, provides a detailed description.

2.5 Adsorption experiment

2.5.1 Dye adsorption

Two anionic organic dyes methyl orange (MO) and congo red (CR), and two cationic dyes, methylene blue (MB) and rhodamine b (RhB), were selected as model dyes to evaluate the adsorption capacity of the composite aerogels. Aerogel samples (20 mg) were put into 50 mL of different anionic and cationic dyes (20 mg/L) and stirred at 200 rpm for adsorption equilibrium.

The pH dependent of the aerogels was performed by adjusting the solution pH range from 3 to 9. Then, the aerogel samples (20mg) were added into 50 mL dye solutions (50 mg/L) at different pH values and stirred at room temperature.

The effect of the experimental temperatures (25°C, 35°C, 45°C) and the coexisting ionic strength (NaCl and Na_2CO_3) on adsorption were studied. Continuous filter adsorption experiments were carried out using a column (25mm in diameter, 20 cm in length) with about 0.2 g RC/CSCA. A solution with anionic (20 mg/L MO) and cationic dye (10 mg/L MB) was percolated through the column via gravity driven.

The adsorption capacity *Qe* (mg/g) and the removal efficiency (*R*) are respectively calculated by the following equations Eq (1) and (2).

$$Q_e = \frac{(C_0 - C_e)V}{m} \quad (1)$$

$$R = \frac{(C_0 - C_e)}{C_0} * 100\% \quad (2)$$

In which, *V* (L) is the volume of the dye solution; C_0 (mg/L) is the initial dye concentration of dye; *m*(g) is the mass of the adsorbent; *Ce* (mg/L) is the equilibrium dye concentration.

2.5.2 Adsorption kinetics

Adsorption kinetic data were obtained by measuring MO's adsorption capacities as a time function. As a result, the pseudo-first order and pseudo-second-order kinetic models can be represented in Eq (3) and (4), respectively.

$$Q_t = Q_e(1 - e^{k_1 t}) \quad (3)$$

$$Q_t = \frac{Q_e^2 k_2 t}{1 + Q_e k_2 t} \quad (4)$$

In which, Q_t (mg/g) Q_e (mg/g) are the adsorption capacity at time t (min) and equilibrium time of absorbent, respectively; k_1 (min^{-1})) and k_2 (g mg^{-1} min^{-1}) are the first-order adsorption rate constant and second-order adsorption rate constant, respectively[14].

The intraparticle diffusion model was also investigated to identify the dye diffusion mechanism and rate-limiting step, as shown in Eq (5).

$$Q_t = k_i \times t^{\frac{1}{2}} + C \quad (5)$$

In which, k_i (mg g^{-1} $min^{-1/2}$) is the intra-particle diffusion rate constant; C is the parameter related to the thickness of the boundary layer [11].

2.5.3 Adsorption isotherms

To obtain adsorption isotherm data, MO adsorption experiments were carried out at initial dye concentrations ranging from 20 to 1000 mg/g (50 mL). The Langmuir and Freundlich models were used to analyze the data obtained. The Langmuir and Freundlich models can be represented in Eq (6) and (7), respectively.

$$Q_e = \frac{C_e K_L Q_{max}}{C_e K_L + 1} \quad (6)$$

$$Q_e = K_F C_e^{\frac{1}{n}} \quad (7)$$

In which, k_L (L/mg) and Q_{max} (mg/g) are the Langmuir constant and the maximum adsorption capacity of absorbent, respectively. K_F[$mg \cdot g^{-1} \cdot (mg \cdot L^{-1})^{-1/n}$]and n are the Freundlich adsorptions constant and the empirical parameter.

2.5.4 Adsorption thermodynamics

The effect of temperature on the adsorption of MO onto RC/CSCA was investigated and the corresponding thermodynamic parameters were calculated. Supplementary Information, Text S2, provides a detailed description.

2.5.5 Reusability

The reusability of the adsorbent was assessed with 20 mg RC/CSCA and 50 ml dye solution (20 mg/L). First, the depleted RC/CSCA was desorbed by soaking in NaOH (0.1M) under agitation, followed by regeneration of the aerogel with 0.1MHCl.

3 **Results and discussion**

3.1 Fabrication and characterization of the aerogel

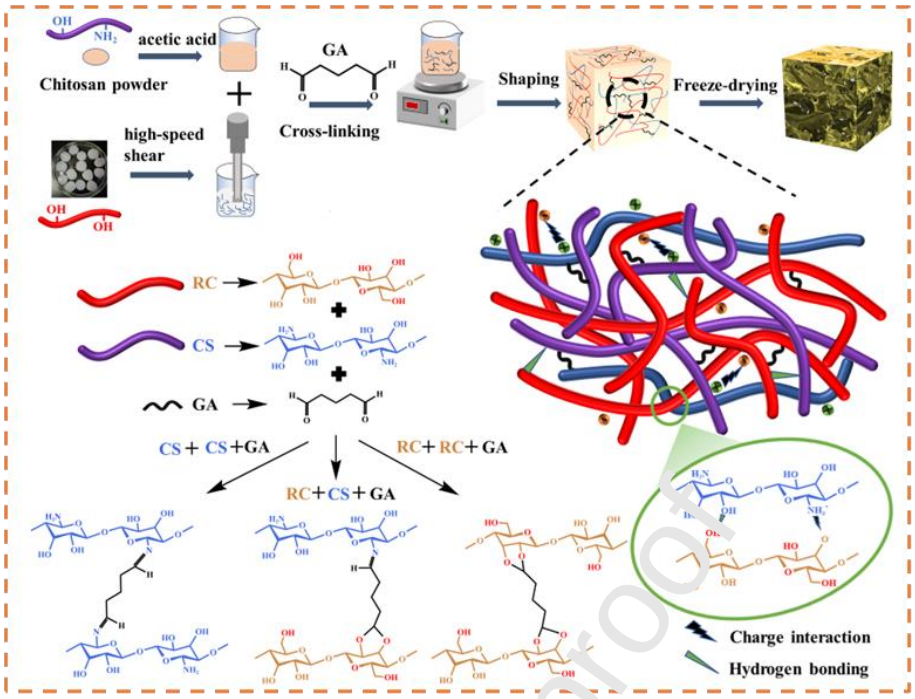

Scheme 1. Schematic diagram of preparation and structure crosslinking of RC/CSCA.

The structural composition and schematic diagram of RC/CSCA are shown in Schema 1. After high-speed shearing, the regenerated cellulose hydrogel (RCH) obtained via NMMO solvent formed a white suspension. Then, CS solution was added into the RCH suspension and mechanically stirred for 1 h at 60℃, while glutaraldehyde (GA) was added drop by drop. The chemical linking reaction triggered among GA, amino group on CS chains, and hydroxyl group on RC formed covalent bonds via the acetal reaction and the Schiff base reaction [30-33], resulting in multiple crosslinked networks. In addition, from the molecular formula of CS, the CS presents abundant $-NH_2$ groups, which can be protonated to $-NH_3^+$ groups in an acid environment. Thus, the CS molecule would be positively charged $-NH_3^+$ groups in an acetic acid solution. CS interacts electrostatically with RC which has a small negative charge on the surface[34]. On the other hand, the cellulose molecule has a large

amount -OH groups, which can combine with CS molecules with hydrogen bonds. Therefore, after combination with CS, the adsorption capacity of RC/CSCA for anionic dyes would be greatly enhanced. The GA forms a stronger bond and reinforces the framework of RC/CSCA via the chemical crosslinking of cellulose and chitosan.

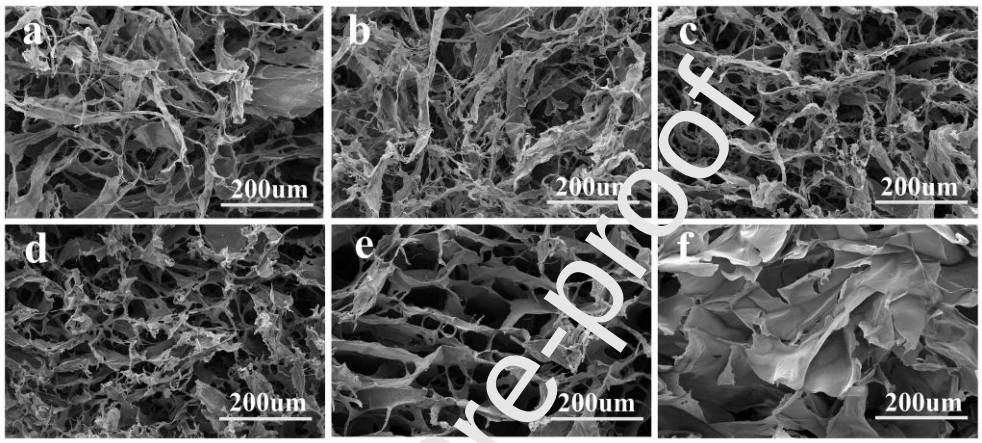

Fig. 1. SEM images of (a) RCA, (b) RC/CSCA-1, (c) RC/CSCA-2, (d) RC/CSCA-3, (e) RC/CSCA-4, and (f) CSA.

From the SEM image of natural cotton pulp shown in Fig S2a, it can be seen that the cotton pulp is composed of abundant rough fibers with a diameter of 10-20 μm. However, after the treatment of NMMO solvent, the strip fibers and flake fibers with a 3D porous structure (Fig. S2b, c) can be observed from the pure regenerated cellulose aerogel (RCA), indicating that the original natural fibers of cotton have been converted to regenerated cellulose. As shown in Fig.S2d, after freeze-drying, the aerogel samples with different mass ration of RC:CS have a typical cylindrical morphology following the template. SEM images of the composite aerogel samples are shown in Fig. 1(a-f). The strip and flake fibers, with a 3D porous structure, are

primarily due to strong hydrogen bonding interactions among the RC fiber. From Fig. 1(b-e), with the addition of chitosan, the pore size of RC/CSCA gradually increases, varying from tens of micrometers to hundreds of micrometers. In addition, more wrinkled CS are covered on the RC fibers, showing that the CS content is essential in forming strong porous structures[28, 35]. Compared with RCA and CSA, the as-prepared RC/CSCA presents large 3D interconnected porous structures, promoting pollutant adsorption. In addition, a distinctive honeycomb pore wall structure can be observed in the RC/CSCA-4 sample. On the other hand, the pure CSA sample is composed of a sheet multi-void structure, as shown in Fig. 1f. The microporous structure of RC/CSCA and CS coating on the surface of RC provide favorable conditions for the rapid adsorption of pollutants.

Fig. 2(a-c) displays the aerogel's water absorption capacity (WAC), density, and porosity with various RC/CS mass ratios. For increasing RC/CS mass ratio from 3:1 to 3:4, the corresponding porosity decreased linearly from 97.36% to 91.36%, and density increased from 15.92 to 26.34 mg/cm^3. As a consequence, due to a large number of hydrophilic groups in CS [23], the WAC of the RC/CSCA sample increased from 36.20 to 44.91g/g. Further increases in CS increased the bulk density, and the WAC decreased to 41.91g/g. Therefore, due to ultra-lightweight, porous structure, and excellent WAC of RC/CSCA, the pollutants (some dyes) can rapidly be adsorbed from water. Furthermore, with the increase of chitosan addition, the density of the 3D porous network of RC/CSCA is much more stable, which limits the swelling space and the water adsorption capacity. On the other hand, the adsorption capacity of

RC/CSCA for anionic dye is mainly based on the chemistry of the -NH_3^+ groups of CS. Therefore, increasing the amount of CS in the RC/CSCA composite means that the more -NH_3^+ groups in the sample can increase the absorption efficiency of dye from water. Moreover, Fig. 2d shows that the obtained RC/CSCA-3 sample has excellent stability and compression performance in the water. It can maintain its original shape after absorbing water and quickly recover after extruding, presenting broad potential in complex water environments [26].

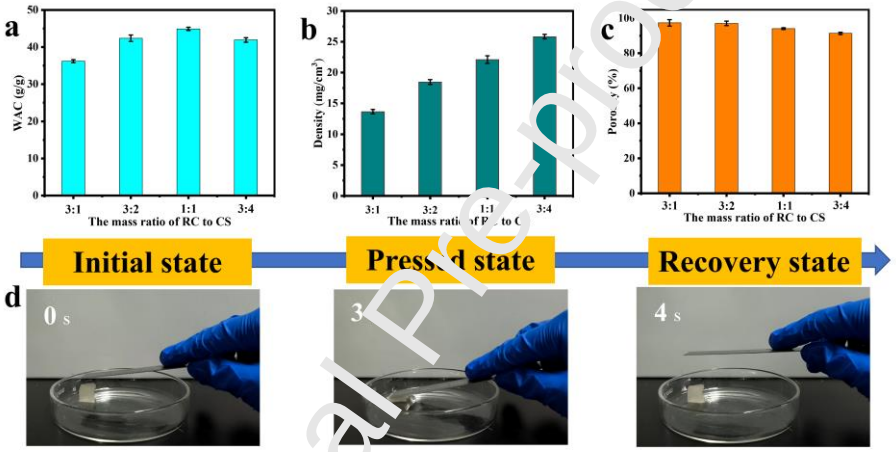

Fig. 2. (a) Water absorption, (b) density, and (c) porosity of RC/CSCA for various RC to CS mass ratios. (d) Photographs of compressed and recovered water-absorbed RC/CSCA-3.

Fig. 3a shows the XRD patterns of raw cotton, RCA, CSA, RC/CSCA-0GA, and RC/CSCA-3 samples. X-ray diffraction of cotton pulps shows the typical cellulose I pattern with peaks at 14.6, 16.1, 22.5, and 34.1°, corresponding to the $(1\bar{1}0)$, (110), (200), and (004) crystal planes [36]. The RCA pattern shows two prominent peaks at 12.2° and 20.4°, corresponding to the (100) and (200) crystal planes, indicating that after NMMO treatment, the cotton structure was transformed to cellulose II[20]. The characteristic diffraction peaks of CSA observed around 19.8° are attributed to the

semi-amorphous phase[37]. When RC combined with CS without GA to form RC/CSCA-0GA, only the peak of RC remained intact, similar to the RC/CSCA-3, indicating that the addition of GA did not affect the crystallinity of the material. However, the intensity of the peaks in RC/CSCA-3 was lower than that of RCA, showing that the added CS hampered the crystal structure formation around the cellulose ribbons, consistent with the SEM image [30].

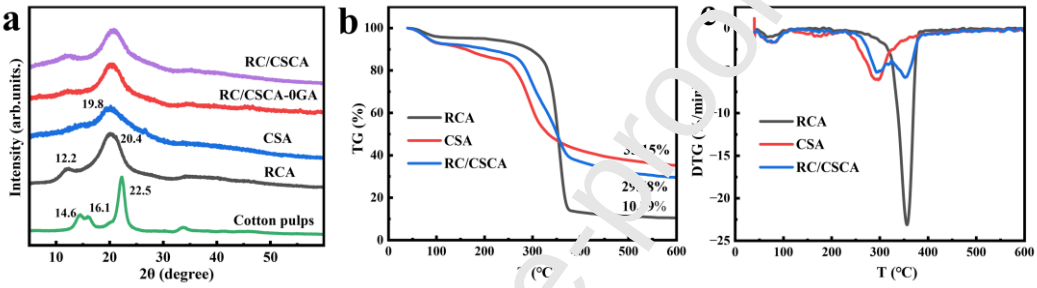

Fig. 3. (a) XRD patterns of Cotton pulps, RCA, CSA, RC/CSCA -0GAand RC/CSCA-3. (b) TG, (c) DTG curves of RCA, CSA, and RC/CSCA-3.

TG and DTG curves of samples are shown in Fig. 3b and c. RCA, CSA, and RC/CSCA-3 samples show a significant mass loss with the temperature increase. Compared with pure RCA, the mass retention rate of RC/CSCA-3 increased from 10.39% to 29.58% at 500°C. After complete carbonization, RC/CSCA-3 has a smaller weight loss than CS due to the introduction of RC. The degradation process could be divided into three steps: first, the evaporation of adsorbed water is responsible for the slight weight loss of about 100°C. The second: the principal weight loss occurs at 200°C-400°C, indicating the glycosidic bond decomposition and the organic compound volatilization. The third: due to the additional thermal degradation carbonization, a slight weight loss was observed at 500°C [38]. The maximum

decomposition rates (T_{max}) of RC/CSCA-3 are 294 and 353°C, corresponding to CS and RC's thermal decomposition, confirming the successful interaction between the two materials.

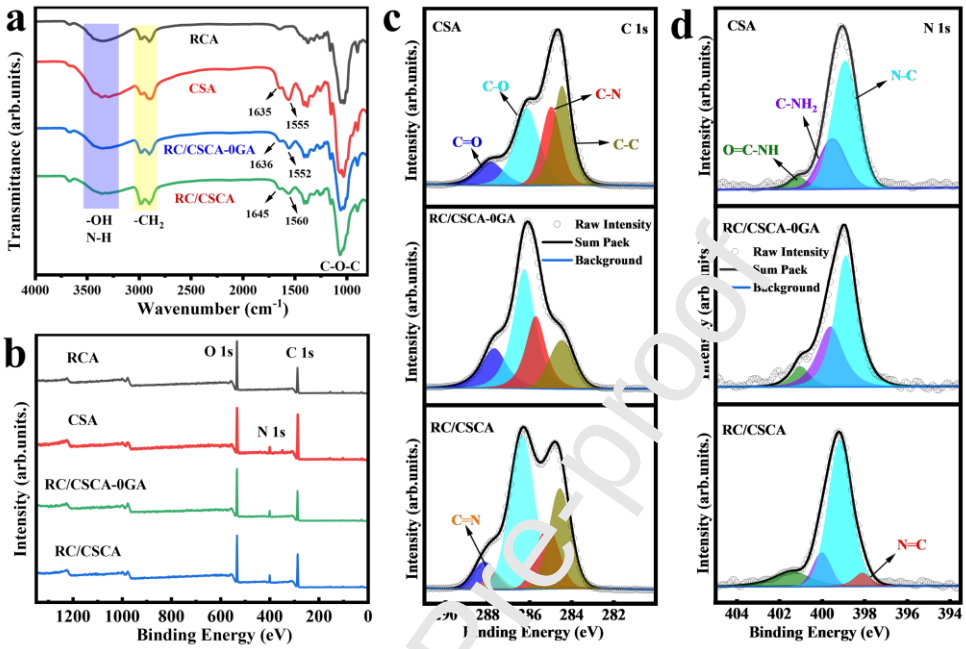

Fig. 4. (a) FTIR spectra (b) Wide-scan XPS of RCA, CSA, RC/CSCA-0GA and RC/CSCA-3. High resolution C 1s (c) and N 1s (d) XPS spectra of RCA, CSA, RC/CSCA-0GA and RC/CSCA-3.

FTIR spectra were used to identify the functional groups of RCA, CSA, RC/CSCA-0GA, and RC/CSCA-3 (Fig. 4a). From the spectra of CSA and RCA, the characteristic peaks corresponding to the asymmetrical tensile vibration of C-O, C-O-C, C-H and-OH groups are observed, indicating that the fundamental structures of chitosan and cellulose materials are preserved[39]. The broad peak at 3351 cm^{-1} is attributed to the overlap of N-H stretching, O-H stretching, and intramolecular hydrogen bond vibration [40, 41]. The weak absorption band at 1635 cm^{-1} is from the stretching vibration of -C=O in the -$NHCOCH_3$ group of CS. The absorption peak at

1555 cm^{-1} is associated with the bending vibration of N-H in the -NH_2 group of CS[42]. Interestingly, after reacting with RC and GA, the corresponding peak shifted to 1645cm^{-1}. In addition, the band of the C=N bond formed through the reaction between -NH_2 groups of CS and -CHO groups of GA also appears in this region, indicating that the Schiff base reaction has occurred[31]. After adding GA, the increased intensity of the peak at 1050-1150 cm^{-1} proved that hydroxyl groups of RC reacted with the aldehyde group of GA to form the O-C-O group[33, 43]. Therefore, suggesting that hydrogen chemical bonds and chemical bonds mainly form the structure of crosslinked RC/CSCA-3.

XPS survey was performed to investigate the elemental composition of RCA, CSA, RC/CSCA-0GA, and RC/CSCA-3, as shown in Fig. 4(b-d). Nitrogen was found in XPS spectra of CSA and RC/CSCA (Fig. 4b) rather than RC, indicating that CS has successfully combined with RC to form aerogel. As shown in Fig. 4c, the RC/CSCA C 1_S broad peak can be fitted with five components: C-C (284.55 eV), C-N (285.14 eV), C-O(286.35eV) C=N (287.38eV), and C=O (288.15 eV). When the crosslinking agent GA was added, the intensity of the component C=N of RC/CSCA-3 increased, indicating the formation of the chemical crosslinking GA with CSA [38, 44]. For RC/CSCA-0GA, the area ratio for the C-O component of C-OH groups to the C-C component is 2.36. After the introduction of GA as a crosslinking agent in RC/CSCA-3, the ratio of the C-O peak to the C-C peak is 1.8, indicating that the hydroxyl aldehyde reaction occurred. This is because -OH groups on the cellulose reacted with GA and formed the acetal groups, leading the C-C (C-C bond in GA) peaks increased

[45]. As shown in Fig. 4d, the RC/CSCA-3 nitrogen peak is composed of four components, including N=C (398.10 eV), N-C (399.15 eV), C-NH_2 (400.00 eV), O=C-NH (401.40 eV). The area ratio N 1s (400.00 eV) /N 1s (401.40 eV) of RC/CSCA is 1, lower than that of CS, equal to 5.17, indicating that part amines react with GA and form imines in RC/CSCA-3 [31]. The analysis of the XPS spectra indicates the successful completion of the Schiff base reaction. The presence of chemical bonds crosslinked with the RC/CSCA-3 is consistent with the results of FTIR.

Furthermore, from the solid-state NMR spectra of RC/CSCA-3 samples with and without glutaraldehyde, as shown in Fig.S3, it can be seen that, compared with the composite aerogel without GA, the peak intensity at C4 of RC/CSCA-3 with GA is reduced, and the chemical shift decreased. This could be explained by the lower mobility of carbon atoms of anhydrous D-glucose units induced by the chemical cross-linking of cellulose with GA[46]. Meanwhile, the reduced area of the signal peaks corresponding to C2, C3, and C5 of the cellulose in the cross-linked RC/CSCA-3 means the number of carbon atoms linking to hydroxyl groups reduced, indicating the acetal reaction occurred between the hydroxyl groups of cellulose and aldehyde groups of GA[47].

Fig. 5a and b show the stress-strain curves of the RC/CSCA-0GA and RC/CSCA samples. These curves show three stages: the first stage (<10%) is the approximate linear elastic region. The second stage belongs to the stress-strain yielding stage in the strain range of 10%-60%, causing structural collapse and partial irreversible damage.

In the third stage (>60%), the densification rapidly increases because the fiber bundles are bent and piled together, causing a steeper curve[48]. The sample with an RC:CS mass ratio of 3:4 exhibits the highest compressive stress, as shown in Fig. 5b. This can be associated with the honeycomb pore wall structure, resulting in a higher vertical compressive stress than the other samples. From the stress-strain curves of RC/CSCA-3 and RC/CSCA-0GA, respectively, samples with and without GA (Fig.5c), it is clear that the mechanical strength of RC/CSCA-3 is significantly improved after the addition of GA, demonstrating that the covalent cross linking of GA with RC and CS improves the mechanical properties of the RC/CSCA-3 composites. Moreover, after ten cycles of stress-strain testing, the RC/CSCA-3 sample presents a good compression recovery performance, as shown in Fig. 5d, suggesting excellent elasticity. The optical images of the damp aerogel sample show that its original shape can be recovered entirely after pressure-releasing, further indicating its excellent compressive and resilience capabilities (Fig. 5e). On the other hand, the excessive vertical load will destroy the internal orientation structure of RC/CSCA-3 (Fig. S4).

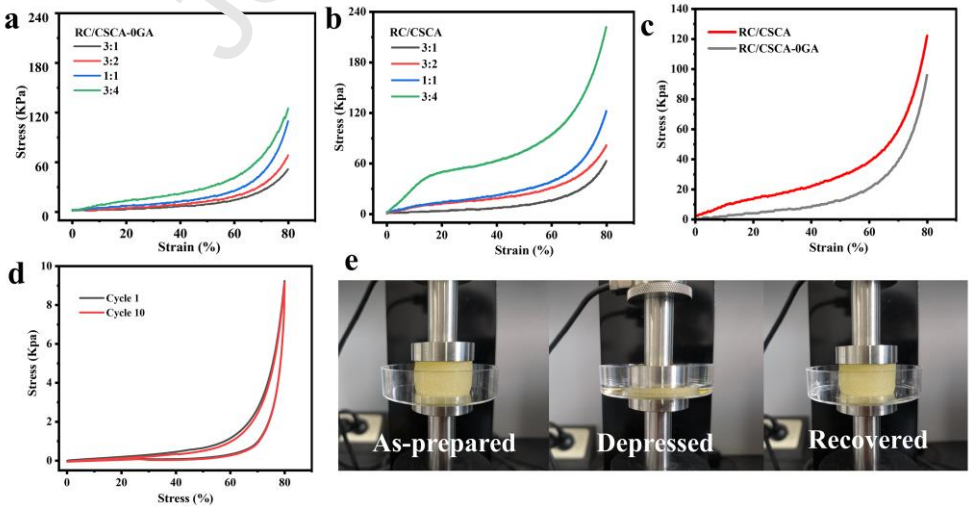

Fig. 5. Stress-strain curve of dry RC/CSCA-0GA (a), and RC/CSCA (b), and the sample with the mass ratio of 1:1 (c), Compression cycle curve of damp RC/CSCA-3 (d); The compressible image of the damp RC/CSCA-3 (e)

As shown in Fig.S5, due to the strong water absorption of chitosan, the amino group combines with a large number of water molecules to form hydrogen bonds, weakening the hydrogen bonds between chitosan and cellulose in the original structure, leading to the damp RC/CSCA-0GA sample collapsed after depressing. Overall, the above results show RC/CSCA-3 with good mechanical properties is suitable for separating contaminants in solutions such as dyes and water in dye solution and reusing.

3.2 Batch adsorption

3.2.1 Dye removal

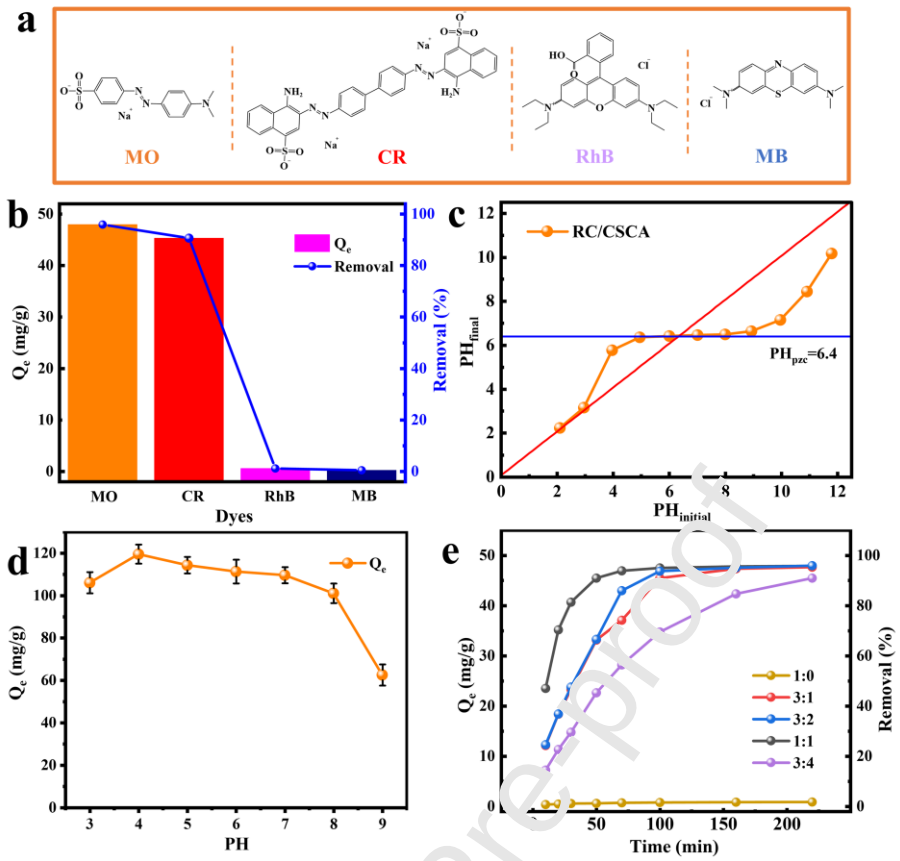

Fig. 6. (a) The structural formulas of the dyes MO, CR, RhB, and MB. (b) R of four different dye types by RC/CSCA-3. (c) pHpzc of RC/CSCA-3. (d) Adsorption capacity changes with PH. (e) Effects of RC/CS mass ratio.

The molecular formulas of the selected dyes to be studied, methyl orange (MO), congo red (CR), rhodamine B (RhB), and methylene blue (MB), are shown in Fig. 6a. The adsorption capacity of RC/CSCA-3 for these dyes is shown Fig.6b. It can be seen that the anionic dyes (MO, CR) were adsorbed to 95.83% and 90.57%, much more effectively than the cationic dyes (RhB, MB), therefore RC/CSCA-3 is suitable for anionic dyes. As is well known, the adsorption capacity of absorbents is seriously influenced by the solution pH because the pH value not only interferes with the surface charge of the adsorbent but also affects the overall chemical properties of the

dye in the solution[13, 49]. In this experiment, we found that the pH at the point of zero charges for the RC/CSCA-3 was 6.40 (Fig. 6c). Therefore, for pH lower or higher than $pH_{PZC,}$ the surface charge of the sample would be negative or positive, respectively [50]. From Fig. 6d, the adsorption capacity of RC/CSCA-3 for MO increased to a maximum at solution pH=4. Further increasing the pH from 4 to 9, the adsorption capacity decreased. Here, we proposed that the protonation of $-NH_2$ groups of CS played an essential role in the interaction between RC/CSCA and MO. In the presence of H^+, the amino group of RC/CSCA is protonated to a positive charge, and the sulfonate groups ($-SO_3H$) of MO dissociate to form an anion ($-SO_3^-$). So, the electrostatic attraction of oppositely charged ions is central to the adsorption process. The adsorption capability of RC/CSCA reduced as the solution pH < 4 because more free hydrogen ions could combine with the negatively charged (SO_3^-) on MO and compete for SO_3^- with NH_3^+ from the adsorbent [29], resulting in the reduction of MO adsorption. However, many more OH^- ions would deprotonate the positive charge of the composite aerogel, weakening the ability to adsorb MO dye because of the electrostatic repulsion between the deprotonated aerogel and the anionic molecule.

The effect of mass ratios of RC to CS of RC/CSCA samples for the adsorption rate and capacity of MO is shown in Fig. 6e and Fig.S6. It can be seen that the RC/CSCA sample with a 1:1 mass ratio of RC to CS presents the optimal adsorption rate and capacity. The removal rate for MO reached 95.83% in 90 min, indicating that the suitable macroporous structure with properly charged functional groups is more favorable to promote the contacting reaction between the active site and dye.

Compared with composites with ratios 3:1, 3:2, and 1:1, the sample with ratio 3:4 contains more CS, therefore more -NH_3^+ groups at the sample surface, resulting in more dye molecules adsorbed and longer adsorption time for reaching the adsorption/desorption equilibrium. However, the dye adsorption capability slightly increased as the CS fraction in the composites increased might be due to the presence of more protonated CS in the composite.

3.2.2 Selectivity

Fig. 7a shows that the intensity of the characteristic adsorption peak at 465 nm of RC/CSCA-3 for MO decreases after adsorption, indicating that most MO molecules were removed from the aqueous solution. However, the pure RCA sample shows a poor adsorption capacity for MO (shown in Fig. S7a), proving that NH_3^+ groups of CS in RC/CSCA can significantly promote the adsorption of MO. Conversely, for the positively charged MB, according to Fig.S7b, the absorption rate decreases slightly after adsorption by RCA, indicating that negatively charged RCA can adsorb a small amount of MB. The MB adsorption curves (λMax =664 nm) before and after RC/CSCA-3 adsorption showed nearly no change because of the electrostatic repulsion, as shown in Fig. 7b, further proving the existence of electrostatic interactions.

A MO and MB mixture solution is used to evaluate the selectivity of RC/CSCA-3 for a mixture of a dye solution (Fig. 7c). Compared with the curve of the mixed MO-MB solution, the intensity of the MO peak centered at 465 nm decreased sharply after RC/CSCA-3 adsorption, rather than that of MB, as well as the color of the mixture

solution changed to blue (the inset in Fig. 7c), indicating that RC/CSCA-3 can only selectively adsorb MO dye from mixed dyes. The adsorption of RC/CSCA-3 for the multiple anionic mixed dyes solution (MO/CR, MO/RhB, and MO/RhB/MB) can be seen in Fig S8. It can be observed that after adsorption, all mixed dye solutions present lighter colors, and the corresponding absorption curves of the dyes in the solution decreased significantly, proving that the composite aerogels can separate multiple anionic dyes from the solution, even if the anionic dye is mixed with other cationic dyes.

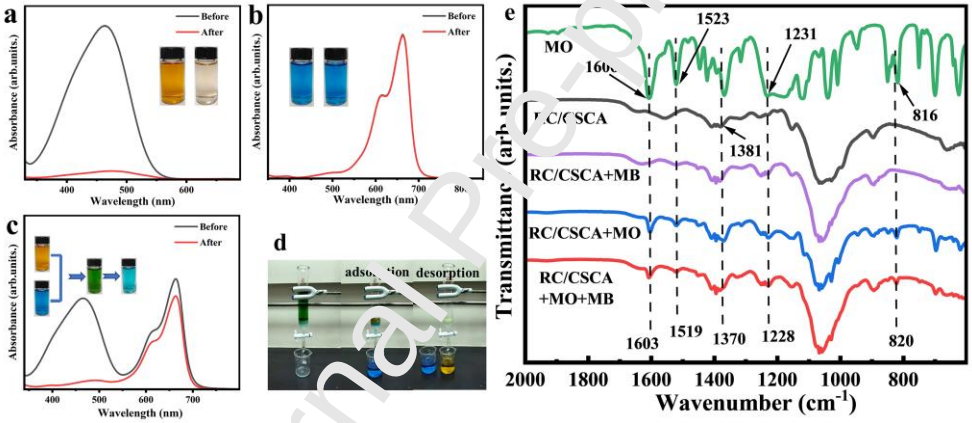

Fig. 7. Absorbance of (a) MO, (b) MB, (c) a mixture of MO/MB before and after adsorption. (d) Filtration separation of MO and MB from mixed solution by RC/CSCA-3, (e) FTIR of RC/CSCA, RC/CSCA + MB, RC/CSCA + MO, and RC/CSCA+ MO+MB aerogel.

The preferential adsorption of RC/CSCA-3 toward anionic dyes was further investigated via the dynamic filtering experiment of a constantly flowing mixed MO/MB solution, as shown in Fig. 7d and Video S1. Under the gravity and the unique 3D pore structure, the dark green MO/MB solution can quickly pass through the RC/CSCA-3 filter, in which the MO molecules were captured and adsorbed on

RC/CSCA-3 because of the abundance of active sites on the pore wall[51]. Then, the filtered solution became blue, showing that the MB were separated. Interestingly, the MO adsorbed on RC/CSCA-3 can be easily desorbed after washing with NaOH solution, offering the better regeneration capability of aerogel materials (Video S2). The result demonstrates that as-prepared RC/CSCA-3 samples have an excellent continuous separating ability from anionic dyes; it provides evidence for the potential application of RC/CSCA in separating flowing mixed dyes.

FTIR spectra of RC/CSCA-3 before and after MO adsorption is shown in Fig. 7e. It can be seen that, after or before MB adsorption, the FTIR pattern of RC/CSCA-3 hardly changed, showing the lower adsorption capacity for MB. However, after MO adsorption, the C-N absorption peak was shifted from 1381cm^{-1} to 1370 cm^{-1} because of the strong interaction between the C-N group and other groups, proving that introducing nitrogen-containing groups is essential for enhancing the adsorption of MO on aerogel. The MO absorption bands of RC/CSCA-3 at 1606cm^{-1}, 1523cm^{-1}, 1231cm$^{-1,}$ and 816cm^{-1} shifted to 1603cm^{-1}, 1519cm^{-1}, 1228cm$^{-1,}$ and 820cm^{-1}, respectively, because C=C bonds in the aromatic ring and C-N and C-H bonds on the benzene ring are involved in the adsorption reaction [27]. Thus, it can be assumed that there is an n-π stacking attraction between the benzene ring and the nitrogen and oxygen with the dye. The resonance absorption peaks of RC/CSCA +MB/MO were similar to those of RC/CSCA +MO, indicating that the presence of MB did not affect the adsorption of MO on RC/CSCA.

3.3. Adsorption mechanism

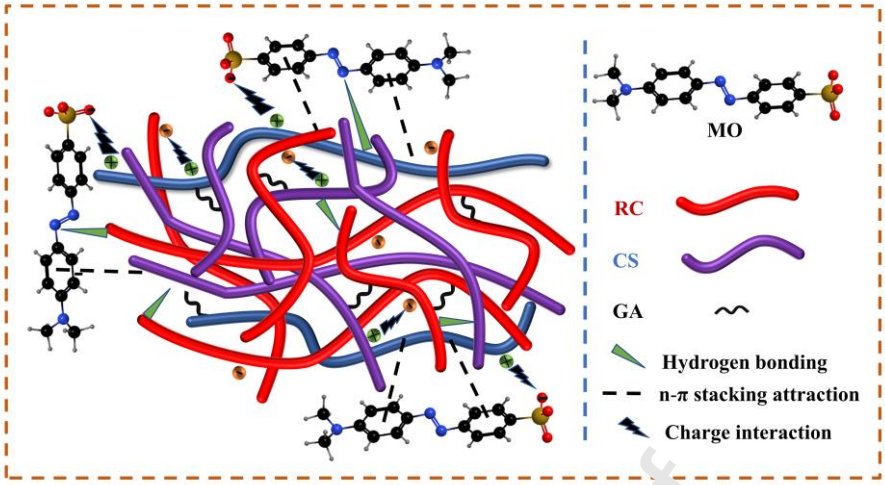

Fig. 8. Schematic diagram of presumed adsorption for MO separation by RC/CSCA

From the above experimental results, the electrostatic interaction, hydrogen, bonds, and n-π stacking attraction were proposed to be the primary driving forces of the adsorption process. Fig. 8 shows the schematic diagram of the electrostatic interaction between the positively charged protonated amino group of RC/CSCA and the negatively charged sulfonate group on MO. The cationic groups ($-NH_3^+$ and $-NH_2^+-$) were generated on the surface of the RC/CSCA after the protonation. Meanwhile, the negatively charged sulfonate group ($-SO_3^-$) can be converted from the sulfonate group ($-SO_3H$) on MO in water[49]. Therefore, $-NH_2^+-$, $-NH_3^+$, and $-SO_3^-$ will produce strong electrostatic attraction, significantly increasing the MO dye adsorption by RC/CSCA. It is also suggested that hydrogen bonds can be formed between the oxygen/nitrogen atoms in MO and the hydrogen on the surface of RC/CSCA. The adsorption of dye molecules on RC/CSCA is a multi-point docking process [52]. Each dye molecule can bind to multiple sites in the RC/CSCA [46]. Therefore, theoretically, the increase of electronegative groups in dyes could enhance

the dye adsorption capacity of RC/CSCA.

3.4 Adsorption kinetic and adsorption isotherm

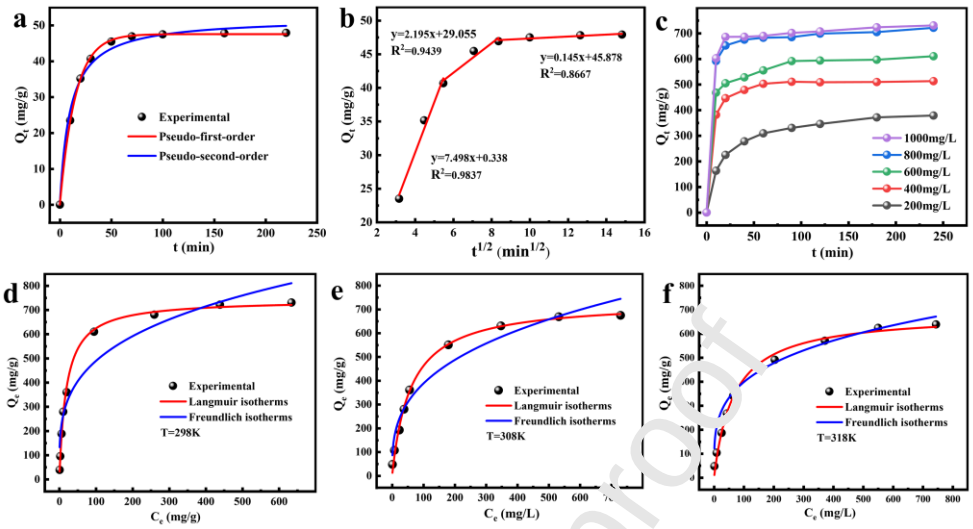

Fig. 9. Kinetic (a), the intra-particle model fit (b), variation of adsorption amount with contact time at different initial dye concentrations (c), experimental data at 298K, 308K, 318K of the isothermal model fitted by RC/CSCA-3 (d-f).

To analyze the kinetics of the adsorption process, the influence of contact time between the adsorbent and MO solution was investigated. From Fig. 9a, the adsorption capacity of the sample for MO increased to 47.91 mg/g after reaching the equilibrium in 90 min. To explain the mechanism of MO adsorption, the experimental data were fitted by non-linear pseudo-first-order kinetic and pseudo-second-order kinetic models. The fitted curves are shown in Fig. 9a. Table 1 lists the parameters calculated after curve fitting. The R^2 values of the fitting curves of the two kinetic processes are higher, indicating that the adsorption of MO by RC/CSCA-3 may be a physical and chemical adsorption process [53].

Fig. 9b shows the effect of different concentrations of dye solution on the

adsorption capacity of the adsorbent. The adsorption capacity increased from 378.83mg/g to 730.90mg/g as the dye concentration increased from 200 mg/L to 1000mg/L. The adsorption rate of the adsorbent was the fastest in the first 20 minutes, and the adsorbent reached the equilibrium state of adsorption and desorption at 90 minutes. The higher initial dye concentration resulted in a higher adsorption capacity, indicating that a stronger driving force from the concentration gradient exists. The initial rapid adsorption is caused by the vacancy interaction between dye molecules and RC/CSCA-3 surface. They are gradually reaching equilibrium with the active adsorbent sites occupied by dyes. Fig. 9c shows the linear relationship between Q_t and $t^{1/2}$ in the adsorption process, indicating that the adsorption process of MO has three stages. The first stage is the rapid transmission of MO in the boundary layer, characterized by strong electrostatic interaction between RC/CSCA-3 and MO. The second stage is due to the mobile diffusion of the dye through the pores of the RC/CSCA-3. In the dye diffusion process, more active sites on the adsorbent are occupied. Due to the repulsion between the adsorbed anionic dye molecules and the identical molecules dispersed in solution, a few remaining sites show greater adsorption resistance. As a result, reaching adsorption equilibrium takes longer, a rate determining step in the dye adsorption process[11]. The region of the third stage of relaxation is the signal for reaching adsorption equilibrium. Additionally, the absence of a straight line through the origin in the model suggests that the adsorption rate is controlled by multiple steps[27].

Moreover, Langmuir adsorption isotherm and Freundlich adsorption isotherm can

be used to study the adsorption mechanism of the adsorbent[54]. The adsorption isotherm fitting curves at different temperatures and associated parameters are shown in Fig. 9(d-f). The adsorption capacity of the adsorbent increases rapidly at low MO concentrations and gradually reaches the maximum after further increasing MO solution concentration. The parameters of the isotherm are in Table 2. The R^2 of the Langmuir model experimental data is better than that of the Freundlich model at all three temperatures. The results showed that MO was adsorbed on the active site of RC/CSCA-3 through monolayer adsorption. The maximum adsorption capacity Q_{max} of RC/CSCA-3 for MO at 298 K is 742.08mg/g, showing good adsorption performance. The calculated values of ΔH^0, ΔS^0, and ΔG^0 are shown in Table S1. Detailed analysis is given in the supporting information. As shown in Table 3, the adsorption capacity of RC/CSCA-3 for MO is compared with that of various CS composites or products. derivatives. It can be proved that RC/CSCA-3 has a high adsorption capacity for MO. This efficient adsorption is due to the electrostatic attraction between the prepared composite and the dye molecules. The results show that the prepared RC/CSCA becomes a promising candidate for removing anionic dyes from mixed dye solutions.

3.5 Effect of environmental conditions

It is necessary to investigate the effects of co-existing ions on MO adsorption because dye wastewater usually contains many ions [55, 56]. Fig. 10a shows the concentrations effect of NaCl and Na_2CO_3 solutions on the adsorption capacity of RC/CSCA-3. With the increased NaCl concentration, the adsorption capacity of

RC/CSCA-3 for MO slightly decreased because Cl^- ions can compete with MO dye molecule for the active site on RC/CSCA-3. CO_3^{2-} as the co-existing ions, can significantly affect MO adsorption capacity because the divalent CO_3^{2-} would compete stronger for positively charged active sites on the adsorbent than that of Cl^- ions.

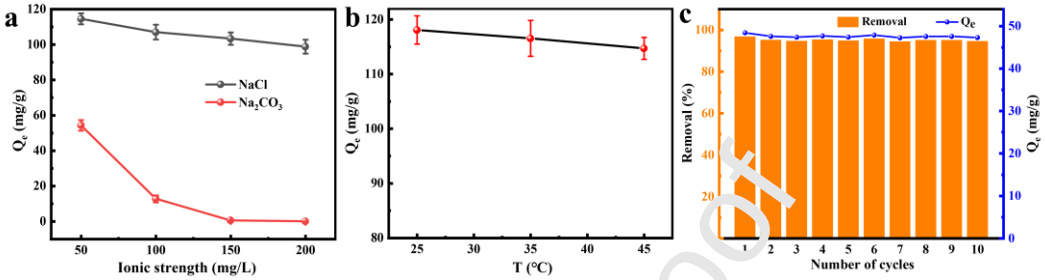

Fig.10. Effect of (a) ionic strength, (b) temperature on MO adsorption capacity. (c) Reusability of RC/CSCA-3 for MO adsorption.

The effect of temperature on MO adsorption from RC/CSCA-3 samples is shown in Fig. 10b. With the increase of temperature from 25℃ to 45℃, the adsorption capacity of MO decreased slightly from 118.07 to 114.71 mg/g, combined with the analytical results of adsorption thermodynamics, indicating that the adsorption process is exothermic[57]. As the kinetic energy of MO molecules increases with increasing temperature, the electrostatic interaction between the MO molecules and the active center on RC/CSCA-3 is weakened. Therefore, regarding energy saving, the prepared adsorbent should be used for wastewater treatment at room temperature.

3.6. Recycle performance.

The recovery and reusability of the absorbent are critical parameters in practical applications. As the surface charge of the RC/CSCA-3 sample is susceptible to the pH of the solution, the adsorbent can be reused for the adsorption process after the

completion of desorption by an alkaline solution and regeneration with an acid solution. Due to the intense competition for adsorption sites between OH^- and adsorbed dyes, NaOH solution can be used to wash the dyes adsorbed on adsorbents[27]. The reusability of RC/CSCA-3 on MO after washing with NaOH solution several times and regenerated in HCl solution is shown in Fig. 10c. After ten cycles, the adsorption capacity only decreases from 95.83% to 94.57%, proving that RC/CSCA-3 sample can be recovered and reused for multiple adsorption-desorption cycles, and is an ideal material for industrial wastewater treatment.

4 CONCLUSIONS

In summary, novel adsorbent RC/CSCA samples were successfully prepared using regenerated cellulose and chitosan as raw materials. The hydrogen bonding and chemical cross-linking among RC, CS, and GA occur, resulting in excellent structural stability and compression performance in the water. Furthermore, due to the protonation of $-NH_2$ groups of CS, RC/CSCA presents a strong selective adsorption capacity for anionic MO dye to 742.68mg/g. Electrostatic interaction was considered the primary means for removing anionic dyes by RC/CSCA, whose efficiency can be above 94.57%c under a wide range of environmental pH. Analysis of the adsorption kinetics and isotherms indicates that the process of MO adsorption by RC/CSCA is a physical chemisorption of a single molecular layer. After ten adsorption-desorption cycles, 94.57% of the adsorption capacity remained, indicating that RC/CSCA can be an ideal material for industrial wastewater treatment.

Acknowledgments

This work was financially supported by Guangxi Key Research and Development Program (2021AB23009), and the National Natural Science Foundation of China (Nos. U1764254 and 21911530255), 111 Project, China (No. D17003). CB thanks the Belgian Fund for Scientific Research under the FRFC contract CDR J001019. CB is a Research Associate of the National Funds for Scientific Research (FRS-FNRS, Belgium).

References

[1] A. James, D. Yadav, Bioaerogels, the emerging technology for wastewater treatment: A comprehensive review on synthesis, properties and applications, Environ. Res. 212 (2022) 113222. https://doi.org/10.1016/j.envres.2022.113222.

[2] N. Fijoł, A. Aguilar-Sánchez, A.P. Mathew, 3D-printable biopolymer-based materials for water treatment: A review, Chem. Eng. J. 430 (2022) 132964. https://doi.org/10.1016/j.cej.2021.132964.

[3] H.I. Syeda, P.S. Yap, A review on three-dimensional cellulose-based aerogels for the removal of heavy metals from water, Sci. Total Environ.t 807 (2022) 150606. https://doi.org/10.1016/j.scitotenv.2021.150606.

[4] E. Sohouli, N. Irannejad, A. Ziarati, H. Ehrlich, M. Rahimi-Nasrabadi, F. Ahmadi, R. Luque, Application of polysaccharide-based biopolymers as supports in photocatalytic treatment of water and wastewater: a review, Environ. Chem. Lett. 20 (2022) 3789–3809 https:// doi.org/10.1007/s10311-022-01456-3.

[5] J. El-Gaayda, F.E. Titchou, R. Oukhrib, P.-S. Yap, T. Liu, M. Hamdani, R. Ait Akbour, Natural flocculants for the treatment of wastewaters containing dyes or heavy metals: A state-of-the-art review, J. Environ. Chem. Eng. 9 (2021) 106060. https://doi.org/10.1016/j.jece.2021.106060.

[6] F. Lu, D. Astruc, Nanomaterials for removal of toxic elements from water, Coordin. Chem. Rev. 356 (2018) 147-164. https://doi.org/10.1016/j.ccr.2017.11.003.

[7] J. Suazo-Hernandez, P. Sepulveda, K. Manquian-Cerda, R. Ramirez-Tagle, M.A. Rubio, N. Bolan, B. Sarkar, N. Arancibia-Miranda, Synthesis and characterization of zeolite-based composites functionalized with nanoscale zero-valent iron for removing arsenic in the presence of selenium from water, J. Hazard. Mater. 373 (2019) 810-819. https://doi.org/10.1016/j.jhazmat.2019.03.125.

[8] R.R. Pawar, Lalhmunsiama, M. Kim, J.-G. Kim, S.-M. Hong, S.Y. Sawant, S.M. Lee, Efficient removal of hazardous lead, cadmium, and arsenic from aqueous environment by iron oxide modified clay-activated carbon composite beads, Appl. Clay Sci. 162 (2018) 339-350. https://doi.org/10.1016/j.clay.2018.06.014.

[9] Y.-X. Ma, D. Xing, C.-P. Lu, X.-Y. Du, F.-Q. La, Preparation of dicyandiamide modified polystyrene resin beads decorated with nano-Fe_3O_4 for removing Hg(II) from aqueous solution, Polym. Compos. 39 (2018) 2232-2240. https://doi.org/10.1002/pc.24187.

[10] R.S. Dassanayake, S. Acharya, N. Abidi, Recent Advances in Biopolymer-Based Dye Removal Technologies, Molecules 26 (2021) 4697-4717. https://doi.org/10.3390/molecules26154697.

[11] C. Feng, P. Ren, M. Huo, Z. Dai, D. Liang, Y. Jin, F. Ren, Facile synthesis of trimethylammonium grafted cellulose foams with high capacity for selective adsorption of anionic dyes from water, Carbohydr. Polym. 241 (2020) 116369. https://doi.org/10.1016/j.carbpol.2020.116369.

[12] N. Aramesh, A.R. Bagheri, M. Bilal, Chitosan-based hybrid materials for adsorptive removal of dyes and underlying interaction mechanisms, Int. J. Biol.

Macromol 183 (2021) 399-422. https://doi.org/10.1016/j.ijbiomac.2021.04.158.

[13] B. Chen, F. Long, S. Chen, Y. Cao, X. Pan, Magnetic chitosan biopolymer as a versatile adsorbent for simultaneous and synergistic removal of different sorts of dyestuffs from simulated wastewater, Chem. Eng. J. 385 (2020) 123926. https://doi.org/10.1016/j.cej.2019.123926.

[14] X. Zhao, X. Wang, T. Lou, Preparation of fibrous chitosan/sodium alginate composite foams for the adsorption of cationic and anionic dyes, J. Hazard. Mater. 403 (2021) 124054. https://doi.org/10.1016/j.jhazmat.2020.124054.

[15] B. Lindman, G. Karlström, L. Stigsson, On the mechanism of dissolution of cellulose, J. Mol. Liq. 156 (2010) 76-81. https://doi.org/10.1016/j.molliq.2010.04.016.

[16] S. Acharya, S. Liyanage, P. Parajuli, S.S. Rumi, J.L. Shamshina, N. Abidi, Utilization of Cellulose to Its Full Potential: A Review on Cellulose Dissolution, Regeneration, and Applications, Polymers (Basel) 13 (2021). https://doi.org/10.3390/polym13244344.

[17] H. Tu, M. Zhu, B. Duan, L. Zhang, Recent Progress in High-Strength and Robust Regenerated Cellulose Materials, Adv. Mater. 33 (2021) e2000682. https://doi.org/10.1002/adma.202000682.

[18] T. Rosenau, A.D. French, N-Methylmorpholine-N-oxide (NMMO): hazards in practice and pitfalls in theory, Cellulose 28 (2021) 5985-5990. https://doi.org/10.1007/s10570-021-03860-4.

[19] V. Rahmanian, T. Pirzada, S. Wang, S.A. Khan, Cellulose-Based Hybrid Aerogels: Strategies toward Design and Functionality, Adv. Mater. 33 (2021)

e2102892. https://doi.org/10.1002/adma.202102892.

[20] Y. Song, S. Zhou, H. Li, F. Xie, H. Yang, Z. Yuan, W. Li, Controllable synthesis of cellulose/methylene bisacrylamide aerogels for enhanced adsorption performance, J. Appl.Polym. Sci. 138 (2020). https://doi.org/10.1002/app.50204.

[21] D. Li, X. Tian, Z. Wang, Z. Guan, X. Li, H. Qiao, H. Ke, L. Luo, Q. Wei, Multifunctional adsorbent based on metal-organic framework modified bacterial cellulose/chitosan composite aerogel for high efficient removal of heavy metal ion and organic pollutant, Chem. Eng. J. 383 (2020) 123127. https://doi.org/10.1016/j.cej.2019.123127.

[22] K.C. Lai, B.Y.Z. Hiew, L.Y. Lee, S. Gan, S. Thangalazhy-Gopakumar, W.S. Chiu, P.S. Khiew, Ice-templated graphene oxide/chitosan aerogel as an effective adsorbent for sequestration of metanil yellow dye, Bioresour. Technol. 274 (2019) 134-144. https://doi.org/10.1016/j.biortech.2018.11.048.

[23] M. Li, X. Li, L. Wang, Y. Pei, M. An, J. Liu, X. Zheng, K. Tang, Highly efficient and selective removal of anionic dyes from water using a cellulose nanofibril/chitosan sponge prepared by dehydrothermal treatment, J. Environ. Chem. Eng. 9 (2021) 105745. https://doi.org/10.1016/j.jece.2021.105745.

[24] E. Salehi, M. Khajavian, N. Sahebjamee, M. Mahmoudi, E. Drioli, T. Matsuura, Advances in nanocomposite and nanostructured chitosan membrane adsorbents for environmental remediation: A review, Desalination 527 (2022). https://doi.org/10.1016/j.desal.2022.115565.

[25] J. Mao, S. Li, C. He, Y. Tang, Z. Chen, J. Huang, Y. Lai, Robust amphiprotic

konjac glucomannan cross-linked chitosan aerogels for efficient water remediation, Cellulose 26 (2019) 6785-6796. https://doi.org/10.1007/s10570-019-02549-z.

[26] N. Rong, C. Chen, K. Ouyang, K. Zhang, X. Wang, Z. Xu, Adsorption characteristics of directional cellulose nanofiber/chitosan/montmorillonite aerogel as adsorbent for wastewater treatment, Sep. Purif. Technol. 274 (2021) 119120. https://doi.org/10.1016/j.seppur.2021.119120.

[27] M.X. Huo, Y.L. Jin, Z.F. Sun, F. Ren, L. Pei, P.G. Ren, Facile synthesis of chitosan-based acid-resistant composite films for efficient selective adsorption properties towards anionic dyes, Carbohydr. Polym. 254 (2021) 117473. https://doi.org/10.1016/j.carbpol.2020.117473.

[28] N.H.N. Do, B.Y. Truong, P.T.X. Nguyen, K.A. Le, H.M. Duong, P.K. Le, Composite aerogels of TEMPO-oxidized pineapple leaf pulp and chitosan for dyes removal, Sep. Purif. Technol. 283 (2022) 120200. https://doi.org/10.1016/j.seppur.2021.120200.

[29] C. Qiu, Q. Tang, X. Zhang, M.-C. Li, X. Zhang, J. Xie, S. Zhang, Z. Su, J. Qi, H. Xiao, Y. Chen, Y. Jiang, C.F. de Hoop, X. Huang, High-efficient double-cross-linked biohybrid aerogel biosorbent prepared from waste bamboo paper and chitosan for wastewater purification, J. Cleaner Prod. 338 (2022) 130550. https://doi.org/10.1016/j.jclepro.2022.130550.

[30] Y. Chen, X. Zhou, Q. Lin, D. Jiang, Bacterial cellulose/gelatin composites: in situ preparation and glutaraldehyde treatment, Cellulose 21 (2014) 2679-2693. https://doi.org/10.1007/s10570-014-0272-9.

[31] D. Zhang, L. Wang, H. Zeng, P. Yan, J. Nie, V.K. Sharma, C. Wang, A three-dimensional macroporous network structured chitosan/cellulose biocomposite sponge for rapid and selective removal of mercury(II) ions from aqueous solution, Chem. Eng. J. 363 (2019) 192-202. https://doi.org/10.1016/j.cej.2019.01.127.

[32] F. Doustdar, A. Olad, M. Ghorbani, Effect of glutaraldehyde and calcium chloride as different crosslinking agents on the characteristics of chitosan/cellulose nanocrystals scaffold, Int. J. Biol. Macromol. 208 (2022) 912-924. https://doi.org/10.1016/j.ijbiomac.2022.03.193.

[33] Q. Chen, Y. Zhao, Q. Xie, C. Liang, Z. Zong, Polyethyleneimine grafted starch nanocrystals as a novel biosorbent for efficient removal of methyl blue dye, Carbohydr. Polym. 273 (2021) 118579. https://doi.org/10.1016/j.carbpol.2021.118579.

[34] F. Zhang, X. Lan, H. Peng, X. Hu, Q. Zhao, A "Trojan Horse" Camouflage Strategy for High-Performance Cellulose Paper and Separators, Adv. Funct. Mater. 30 (2020). https://doi.org/10.1002/adfm.202002169.

[35] T. Dong, N. Tian, B. Xu, X. Huang, S. Chi, Y. Liu, C.W. Lou, J.H. Lin, Biomass poplar catkin fiber-based superhydrophobic aerogel with tubular-lamellar interweaved neurons-like structure, J. Hazard. Mater. 429 (2022) 128290. https://doi.org/10.1016/j.jhazmat.2022.128290.

[36] H. Yuan, J. Wu, D. Wang, L. Huang, L. Chen, S. Lin, Ultra-high-strength composite films prepared from NMMO solutions of bamboo-derived dissolving pulp and chitosan, Ind. Crop. Prod. 170 (2021). https://doi.org/10.1016/j.indcrop.2021.113747.

[37] F. Tian, Y. Liu, K. Hu, B. Zhao, The depolymerization mechanism of chitosan by hydrogen peroxide, J. Mater. Sci. 38 (2003) 4709-4712.

[38] J. Zhu, R. Xiong, F. Zhao, T. Peng, J. Hu, L. Xie, H. Xie, K. Wang, C. Jiang, Lightweight, High-Strength, and Anisotropic Structure Composite Aerogel Based on Hydroxyapatite Nanocrystal and Chitosan with Thermal Insulation and Flame Retardant Properties, ACS Sustain. Chem. Eng. 8 (2019) 71-83. https://doi.org/10.1021/acssuschemeng.9b03953.

[39] M. Zhang, S. Jiang, F. Han, M. Li, N. Wang, L. Liu, Anisotropic cellulose nanofiber/chitosan aerogel with thermal management and oil absorption properties, Carbohydr. Polym. 264 (2021) 118033. https://doi.org/10.1016/j.carbpol.2021.118033.

[40] Y. Liu, Y. Ke, Q. Shang, X. Yang, D. Wang, G. Liao, Fabrication of multifunctional biomass-based aerogel with 3D hierarchical porous structure from waste reed for the synergetic adsorption of dyes and heavy metal ions, Chem. Eng. J. 451 (2023) 138934. https://doi.org/10.1016/j.cej.2022.138934.

[41] Z.-H. Wu, X.-L. Peng, Y.-X. Qu, L.-X. Gong, K. Cao, G.-D. Zhang, Y. Shi, J.-F. Gao, P. Song, L.-C. Tang, Silane modified MXene/polybenzazole nanocomposite aerogels with exceptional surface hydrophobicity, flame retardance and thermal insulation, Compos. Commun. 37 (2023). https://doi.org/10.1016/j.coco.2022.101402.

[42] Z.-H. Zhang, Z.-Y. Chen, Y.-H. Tang, Y.-T. Li, D. Ma, G.-D. Zhang, R. Boukherroub, C.-F. Cao, L.-X. Gong, P. Song, K. Cao, L.-C. Tang, Silicone/graphene oxide co-cross-linked aerogels with wide-temperature mechanical flexibility, super-hydrophobicity and flame resistance for exceptional thermal insulation and oil/water

separation, J. Mater. Sci. Technol. 114 (2022) 131-142. https://doi.org/10.1016/j.jmst.2021.11.012.

[43] Y.-X. Qu, K.-Y. Guo, H.-T. Pan, Z.-H. Wu, B.-F. Guo, X.-L. Feng, T.-T. Kong, C. Zhang, G.-D. Zhang, L. Zhao, L.-X. Gong, J.-F. Gao, H.-L. Liu, Z.-N. Mao, L.-C. Tang, Facile synthesis of mechanically flexible and super-hydrophobic silicone aerogels with tunable pore structure for efficient oil-water separation, Mater. Today Chem. 26 (2022). https://doi.org/10.1016/j.mtchem.2022.101068.

[44] C. Zhang, Z. Chen, W. Guo, C. Zhu, Y. Zou, Simple fabrication of Chitosan/Graphene nanoplates composite spheres for efficient adsorption of acid dyes from aqueous solution, Int. J. Biol. Macromol 112 (2018) 1048-1054. https://doi.org/10.1016/j.ijbiomac.2018.02.074.

[45] C. Santillo, Y. Wang, G.G. Buonocore, G. Gentile, L. Verdolotti, S. Kaciulis, H. Xia, M. Lavorgna, Hybrid Graphenene Oxide/Cellulose Nanofillers to Enhance Mechanical and Barrier Properties of Chitosan-Based Composites, Front. Chem. 10 (2022) 926364. https://doi.org/10.3389/fchem.2022.926364.

[46] C. Chang, L. Zhang, J. Zhou, L. Zhang, J.F. Kennedy, Structure and properties of hydrogels prepared from cellulose in NaOH/urea aqueous solutions, Carbohydr. Polym. 82 (2010) 122-127. https://doi.org/10.1016/j.carbpol.2010.04.033.

[47] Q. Yang, J. Guo, Y. Liu, F. Guan, J. Song, X. Gong, Improved Properties of Cellulose/Antarctic Krill Protein Composite Fibers with a Multiple Cross-Linking Network, Adv. Fiber Mater. 4 (2021) 256-267. https://doi.org/10.1007/s42765-021-00103-w.

[48] J. Huang, D. Li, M. Zhao, H. Ke, A. Mensah, P. Lv, X. Tian, Q. Wei, Flexible electrically conductive biomass-based aerogels for piezoresistive pressure/strain sensors, Chem. Eng. J. 373 (2019) 1357-1366. https://doi.org/10.1016/j.cej.2019.05.136.

[49] D. Shu, F. Feng, H. Han, Z. Ma, Prominent adsorption performance of amino-functionalized ultra-light graphene aerogel for methyl orange and amaranth, Chem. Eng. J. 324 (2017) 1-9. https://doi.org/10.1016/j.cej.2017.04.136.

[50] S.G. Muntean, M.A. Nistor, R. Ianoș, C. Păcurariu, A. Căpraru, V.-A. Surdu, Combustion synthesis of Fe_3O_4/Ag/C nanocomposite and application for dyes removal from multicomponent systems, Appl. Surf. Sci. 481 (2019) 825-837. https://doi.org/10.1016/j.apsusc.2019.03.161.

[51] W. Zhang, L. Wang, E. Mäkilä, S. Willför, C. Xu, Ultralight and porous cellulose nanofibers/polyethyleneimine composite aerogels with exceptional performance for selective anionic dye adsorption, Ind. Crop. Prod. 177 (2022) 114513. https://doi.org/10.1016/j.indcrop.2021.114513.

[52] L. Zhang, L. Seffaoui, D. Franco, G.L. Dotto, A. Bajahzar, H. Belmabrouk, A. Bonilla-Petriciolet, M.L.S. Oliveira, Z. Li, Adsorption of dyes brilliant blue, sunset yellow and tartrazine from aqueous solution on chitosan: Analytical interpretation via multilayer statistical physics model, Chem. Eng. J. 382 (2020) 122952. https://doi.org/10.1016/j.cej.2019.122952.

[53] Y. Liu, H. Xu, Equilibrium, thermodynamics and mechanisms of Ni^{2+} biosorption by aerobic granules, Biochem. Eng. J. 35 (2007) 174-182.

https://doi.org/10.1016/j.bej.2007.01.020.

[54] J. Wang, X. Guo, Adsorption kinetic models: Physical meanings, applications, and solving methods, J Hazard Mater 390 (2020) 122156. https://doi.org/10.1016/j.jhazmat.2020.122156.

[55] A.G. Varghese, S.A. Paul, M.S. Latha, Remediation of heavy metals and dyes from wastewater using cellulose-based adsorbents, Environ. Chem. Lett. 17 (2018) 867-877. https://doi.org/10.1007/s10311-018-00843-z.

[56] D.-M. Guo, Q.-D. An, R. Li, Z.-Y. Xiao, S.-R. Zhai, Ultrahigh selective and efficient removal of anionic dyes by recyclable polyethylenimine-modified cellulose aerogels in batch and fixed-bed systems, Colloid. Surface. A 555 (2018) 150-160. https://doi.org/10.1016/j.colsurfa.2018.06.081.

[57] J. Yang, J. Wang, X. Zhang, M. Chen, B. Tian, N. Wang, X. Huang, H. Hao, Exploration of hydrogen-bonded organic framework (HOF) as highly efficient adsorbent for rhodamine B and methyl orange, Microporous Mesoporous Mat. 330 (2022). https://doi.org/10.1016/j.micromeso.2021.111624.

[58] J. Tang, Y. Song, F. Zhao, S. Spinney, J. da Silva Bernardes, K.C. Tam, Compressible cellulose nanofibril (CNF) based aerogels produced via a bio-inspired strategy for heavy metal ion and dye removal, Carbohydr Polym 208 (2019) 404-412. https://doi.org/10.1016/j.carbpol.2018.12.079.

[59] W. Song, M. Zhu, Y. Zhu, Y. Zhao, M. Yang, Z. Miao, H. Ren, Q. Ma, L. Qian, Zeolitic imidazolate framework-67 functionalized cellulose hybrid aerogel: an environmentally friendly candidate for dye removal, Cellulose 27 (2019) 2161-2172.

https://doi.org/10.1007/s10570-019-02883-2.

[60] K. Rathinam, S.P. Singh, C.J. Arnusch, R. Kasher, An environmentally-friendly chitosan-lysozyme biocomposite for the effective removal of dyes and heavy metals from aqueous solutions, Carbohydr Polym 199 (2018) 506-515. https://doi.org/10.1016/j.carbpol.2018.07.055.

[61] E. Wi, S. Go, S.Y. Shin, H.J. Cheon, G. Jeong, H. Cheon, J. Kim, H.-R. Jung, H. Kim, M. Chang, Highly efficient and selective removal of anionic dyes from aqueous solutions using magneto-responsive Fe-aminoclay/Fe_2O_3/polyvinyl alcohol composite microgels, Chem. Eng. J. 454 (2023). https://doi.org/10.1016/j.cej.2022.140309.

[62] N. Grishkewich, Y. Li, K. Liu, K.C. Tam, Synthesis and characterization of modified cellulose nanofibril organosilica aerogels for the removal of anionic dye, J. Polym. Res. 29 (2022). https://doi.org/10.1007/s10965-022-03102-6.

[63] L. Jiang, X. Hu, B. Yang, Z. Yang, C. Lu, Preparation of porous diethylene triamine reduced graphene oxide aerogel for efficient pollutant dye adsorption, J. Porous Mat. (2023). https://doi.org/10.1007/s10934-023-01436-0.

[64] S.Z. Hu, Y.F. Deng, L. Li, N. Zhang, T. Huang, Y.Z. Lei, Y. Wang, Biomimetic Polylactic Acid Electrospun Fibers Grafted with Polyethyleneimine for Highly Efficient Methyl Orange and Cr(VI) Removal, Langmuir 39 (2023) 3770-3783. https://doi.org/10.1021/acs.langmuir.2c03508.

Table 1. On the kinetic parameters of RC/CSCA-3 adsorption of MO.

		Pseudo-first-order			Pseudo-second order		
C_0 ($mg \cdot L^{-1}$)	Q_e (exp) ($mg \cdot g^{-1}$)	K_1 (1/min)	Q_e (eal) ($mg \cdot g^{-1}$)	R^2	K_2 ($g \cdot mg^{-1} \cdot min^{-1}$)	Q_e (eal) ($mg \cdot g^{-1}$)	R^2
20	47.92	6.67×10^{-2}	47.55	0.9997	1.93×10^{-3}	52.11	0.9902
200	378.83	4.84×10^{-2}	351.59	0.9720	1.63×10^{-4}	395.29	0.9973
400	513.35	1.32×10^{-1}	502.99	0.9941	5.19×10^{-4}	525.62	0.9993
600	610.72	1.50×10^{-1}	575.82	0.9762	4.90×10^{-4}	603.37	0.9936
800	721.92	1.80×10^{-1}	692.27	0.9950	6.92×10^{-4}	712.33	0.9989
1000	730.90	1.90×10^{-1}	706.69	0.9963	7.40×10^{-4}	724.83	0.9975

Table 2. Fitting parameters for MO sorption isotherms on RC/CSCA-3.

		Langmuir isotherms			Freundlich isotherms		
T	Q_{max}(exp)	Q_{max}	k_L	R^2	k_F	n	R^2
(k)	(mg/g)	(mg/g)	(L/mg)		(mg/g)		
298	730.90	742.68	5.30×10^{-2}	0.9979	138.70	3.65	0.9181
308	674.71	735.70	1.68×10^{-2}	0.9946	85.74	0.32	0.9549
318	638.44	684.53	1.50×10^{-2}	0.9916	120.12	0.26	0.9197

Table 3. Comparison of different adsorbents for maximum MO adsorption.

Adsorbents	Adsorption capacity (mg/g)	References
Regenerated cellulose/ Chitosan composite aerogel	742.68	This work
Cellulose nanofiber/Chitosan films	655.23	2021 [27]
TEMPO-oxidized cellulose/chitosan aerogel	136.34	2022l [28]
Cellulose nanofibril/polyethylenimine aerogel	265.90	2019[58]
ZIF-67/cellulose composite aerogel	617.00	2019[59]
Chitosan/Graphene nanoplates composite	230.91	2018[44]
Chitosan-lysozyme biocomposite	435.00	2018[60]
Fe-AC/Fe_2O_3/PVA microgel	457.31	2023[61]
DADMAC-MBAA modified CNF-Silica aerogels	186.7	2022[62]
Diethylene triamine reduced graphene oxide aerogel	227.24	2022[63]
sc-PLA/PDA/PEI Composite Fibers	612	2023[64]

CRediT authorship contribution statement

Shaochun He: Conceptualization, Data Curation, Methodology, Formal analysis, Writing - Original Draft; **Junting Li:** Formal analysis, Writing - Review & Editing; **Xundan Cao:** Formal analysis, Writing - Review & Editing; **Fei Xie:** Methodology, Supervision, Formal analysis, Writing - Review & Editing; **Hui Yang:** Writing - Review & Editing; **Cheng Wang:** Writing - Review & Editing; **Carla Bittencourt:** Writing - Review & Editing; **Wenjiang Li:** Conceptualization, Methodology, Formal analysis, Funding acquisition, Supervision, Writing - Review & Editing;

Declaration of competing interest

The authors declare that they have no known competing financial interests or personal relationships that could have appeared to influence the work reported in this paper.

Graphical abstract

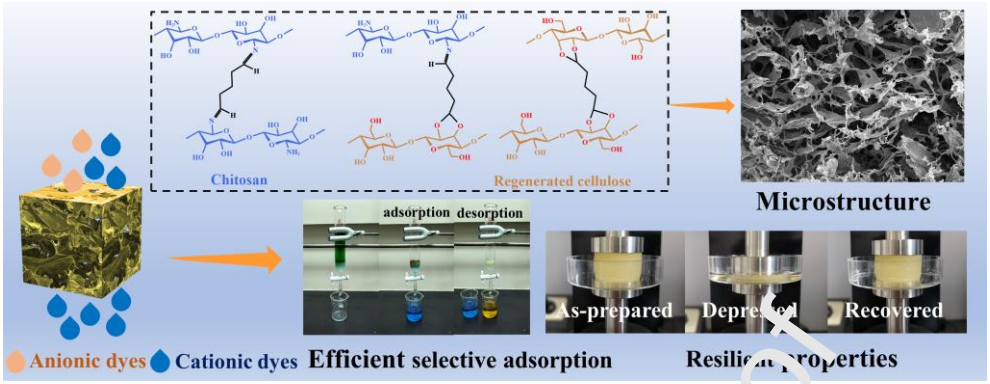

Research Highlights

- A Novel porous regenerated cellulose/chitosan composite aerogel was prepared.
- Stability of composite aerogel was enhanced by the potentiation of chemical crosslinking.
- The aerogel shows selective adsorption of anionic dyes when coexisting with cationic dyes.
- FTIR revealed the selective adsorption mechanism mainly via electrostatic interaction.